Residual flow and tidal asymmetry in the Singapore Strait, with implications for resuspension and residual transport of sediment

D. S. van Maren[1,2] and H. Gerritsen[1]

Received 28 September 2011; revised 10 February 2012; accepted 15 February 2012; published 11 April 2012.

[1] The Singapore Strait connects the South China Sea, where tides are dominantly diurnal, to the dominantly semidiurnal Indian Ocean. At this transition, the tidal water level oscillations are observed to be semidiurnal while the tidal current oscillations are mixed, diurnal to fully diurnal. Due to the interaction of the diurnal constituents with the semidiurnal M_2 tide, the tides are strongly asymmetric. Both residual flows and subtidal flows, with periodicities of 2 weeks to 1 year, are strong. In order to analyze and explain the hydrodynamics around Singapore, a well-documented and calibrated regional tidal model application was further improved and validated. Analysis of the results of this model shows that the diurnal tidal wave is primarily standing, with an amphidromic point close to Singapore, explaining the dominantly diurnal current and semidiurnal water level oscillations. Analysis of the model results further indicates that the fortnightly constituents in the subtidal flow are probably compound tides, with a combined amplitude over 10 cm/s. Pronounced yearly and half-yearly cycles in spring tidal current amplitude and asymmetry exist, resulting from interaction of the diurnal and the semidiurnal spring-neap cycles, compound tides, and the monsoon currents. A simple analytical transport formula was applied to determine the relative importance of tidal asymmetry and residual flows, verified with a full sediment transport model. With fine sediment being more sensitive for residual flow and coarser sediment for tidal flow, a pronounced divergence in sediment transport pathways may exist, depending on the grain size.

Citation: van Maren, D. S., and H. Gerritsen (2012), Residual flow and tidal asymmetry in the Singapore Strait, with implications for resuspension and residual transport of sediment, *J. Geophys. Res.*, *117*, C04021, doi:10.1029/2011JC007615.

1. Introduction

[2] The oceanography of the South China Sea (SCS) region is among the most complex in the world. The SCS region consists of deep basins connected to shallow ridges or narrow straits, numerous semienclosed seas, several large and numerous smaller islands, rapidly varying topography, and rugged coastlines. The water motion is driven by the Indian and Pacific Ocean tides, and the Monsoon winds. The larger part of the SCS has a diurnal tidal regime or is mixed, predominantly diurnal. Knowledge on the tides and the Monsoon-driven throughflow has increased substantially in the past half century, from the pioneering work of *Wyrtki* [1961], based on water level and current data, to more detailed studies using satellite altimetry [*Mazzega and Berge*, 1994; *Schrama and Ray*, 1994; *Ray et al.*, 2005], observations [*Potemra et al.*, 2002; *Gordon*, 2005] and numerical models [*Ye and Robinson*, 1983; *Hatayama et al.*, 1996; *Robertson and Field*, 2005; *Robertson*, 2011]. However, the detailed tidal current dynamics in the straits around Singapore, connecting the SCS with the Andaman Sea through the Malacca, Durian, and Singapore Straits, is comparatively poorly known.

[3] Singapore is located on the transition between the dominantly semidiurnal Indian Ocean and the mixed to diurnal South China Sea, resulting in a complex mix of semidiurnal and diurnal current and water level oscillations. The local water level oscillations are semidiurnal while the current oscillation is dominantly diurnal, which was attributed to the presence of a diurnal amphidrome and a semidiurnal antiamphidrome by *Pugh* [1987]. Especially compared to the overwhelming literature on tidal asymmetry in semidiurnal regimes, investigations of tidal asymmetry in the diurnal or mixed, dominantly diurnal tidal regime are less common. Most of the areas where diurnal tides occur (see *Hoitink et al.* [2003] for a global distribution) are by now documented in scientific literature: the Northern Gulf of Mexico [*Seim and Sneed*, 1988], Australia [*Ranasinghe and Pattiaratchi*, 2000; *O'Callaghan et al.*, 2010; *Jewell et al.*, 2012], and the South China Sea (the Java Sea: *Hoitink and Hoekstra* [2003]; and the Gulf of Tonkin: *van Maren and Hoekstra* [2004] and *van Maren et al.* [2004]). Detailed studies on the transition between diurnal to semidiurnal

[1]Deltares, Delft, Netherlands.
[2]Section of Hydraulic Engineering, Delft University of Technology, Delft, Netherlands.

0148-0227/12/2011JC007615

regimes are so far lacking, which is filled with the work presented here.

[4] Our understanding of the tidal asymmetry in diurnal or mixed tidal regimes has advanced significantly since the work of *Ranasinghe and Pattiaratchi* [2000], who first addressed this issue. They concluded that in inlets in a diurnal tidal regime, tidal asymmetry is dictated by oceanic forcing. However, another of their conclusions, that simple phase angle relationships to predict flood/ebb dominance cannot be derived for diurnal tidal systems, was proven incorrect by *Hoitink et al.* [2003], who demonstrated that a persistent asymmetry can be generated by the O_1-K_1-M_2 triad. *van Maren et al.* [2004] showed that this asymmetry may lead to pronounced morphological changes. The degree of asymmetry, however, fluctuates throughout the year because of the S_2 constituent [*O'Callaghan et al.*, 2010, *Jewell et al.*, 2012]. A topic poorly addressed in scientific literature is that mixed tidal regimes have relatively strong fortnightly tidal constituents at multiple frequencies. The water level amplitude of the fortnightly constituents is particularly high in the South China Sea, with amplitudes typically 2–4 times higher than the average for the tropics, and even more compared to midlatitudes [*Egbert and Ray*, 2003]. These amplitudes may be sufficiently large to substantially influence the tidal dynamics.

[5] *Hoitink et al.* [2003] developed a method to quantify the degree of asymmetry based on the O_1-K_1-M_2 triad, which is especially suitable in areas where the diurnal constituents are dominant. In areas where the semidiurnal constituents are also pronounced, and the M_2-M_4 asymmetry is significant, probability density distributions [*Woodworth et al.*, 2005], or skewness [*Nidzieko*, 2010] are more suitable. Nidzieko's method was generalized by *Song et al.* [2011], to include all tidal constituents and identify the contributions of multiple pairs or triplets of tidal constituents. Analyzing 355 water level stations distributed worldwide revealed that the O_1-K_1-M_2 triad is the most important source of tidal asymmetry by astronomical forcing. Only in purely semidiurnal tidal regimes does the friction-generated M_2-M_4 pair contribute more to tidal asymmetry than O_1-K_1-M_2: even in the mixed, mainly semidiurnal regime the O_1-K_1-M_2 was observed to be the dominant source of tidal asymmetry in 73% of the stations with significant asymmetry.

[6] An important advantage of Hoitink's analytical method is that it allows for an estimate of the effect of asymmetry on sediment transport (as in the work of *Hoitink et al.* [2003]), but also a distinction of transport generated by tidal asymmetry and by residual flow [*van Maren et al.*, 2004]. Most studies on transport of sediment by tidal asymmetry focus on the semidiurnal tidal regime [*Dronkers*, 1986; *Friedrichs and Aubrey*, 1988; *van de Kreeke and Robaczewska*, 1993; *Ridderinkhof*, 1997], in particular that of the M_2–M_4 interaction. Quantitative investigations of sediment transport by tidal asymmetry in the diurnal regime are scarce. The aim of this paper is to analyze and explain the tidal and subtidal motions in the Singapore Strait, and to identify their combined effect on the resuspension and residual transport of sediment. The hydrodynamics of the South China Sea are briefly introduced in section 2, followed by a detailed analysis of tidal dynamics and residual flows in Singapore's coastal waters. Implications for residual bed load transport are evaluated in section 4, while results are generalized in the discussion, section 5.

2. Hydrodynamics of the South China Sea

[7] The South China Sea is located in-between the Philippines, China, Vietnam, Thailand, the Malay Peninsula, and the island of Borneo (Figure 1); south of the South China Sea are the Indonesian Seas. Of particular interest for the flow dynamics around Singapore is the Karimata Strait, in-between the Malay Peninsula and Borneo, which connects to the Java Sea. For simplicity, we will refer to both the South China Sea and the Indonesian Seas as the South China Sea. The currents in the South China Sea are primarily forced by the annual variation of the Monsoon winds and by tides with a pronounced spatially varying dominance of semidiurnal and diurnal constituents.

2.1. Monsoon Driven Currents

[8] The Monsoon winds are generated by a combination of the trade winds and the seasonal variation of the position of the sun. Near the equator, the trade winds generate a persistent system of easterly winds. The resulting pressure gradient between the western Pacific and the eastern Indian Ocean drives a net westward flow through the South China Sea. The equatorial pressure trough moves according to the position of the sun, crossing the equator twice each year, generating a North-South component of the wind direction. November to April is dominated by the Northeast monsoon (north of the equator) and the Northwest monsoon south of the equator (between 0° and 10°S). May to October is dominated by the Southeast monsoon (south of the equator) or the Southwest monsoon north of the equator (between 0° and 10°N) [*Wyrtki*, 1961].

[9] November to April is dominated by the Northeast Monsoon (north of the equator) and the Northwest Monsoon south of the equator (between 0° and 10°S). May to October is dominated by the Southeast Monsoon (south of the equator) or the Southwest Monsoon north of the equator (between 0° and 10°N) [*Wyrtki*, 1961]. As a result, the sea level near Singapore fluctuates over 40 cm annually, with lowest levels in June–July and a peak in November [*Wyrtki*, 1961]. The flow in the Singapore Strait is generally westward throughout most of the year, with velocities of 10–15 cm/s, but flows eastward during the peak of the SW Monsoon, from June until August [*Robinson et al.*, 1953; *Kow*, 1973]. The persistent westward flow is generated by the water level gradient between the Andaman Sea and the South China Sea [*Wyrtki*, 1961]. The water level in the Andaman Sea is always lower than in the South China Sea, driving a net flow from the South China Sea into the Malacca Strait. The water level oscillations result from the basin-wide response to the Monsoon winds, and therefore this persistent westward flow is indirectly related to the Monsoon winds.

2.2. Tides

[10] The tides in the South China Sea are influenced by semidiurnal tides (mainly the principal solar component S_2 and the principal lunar component M_2), as well as diurnal

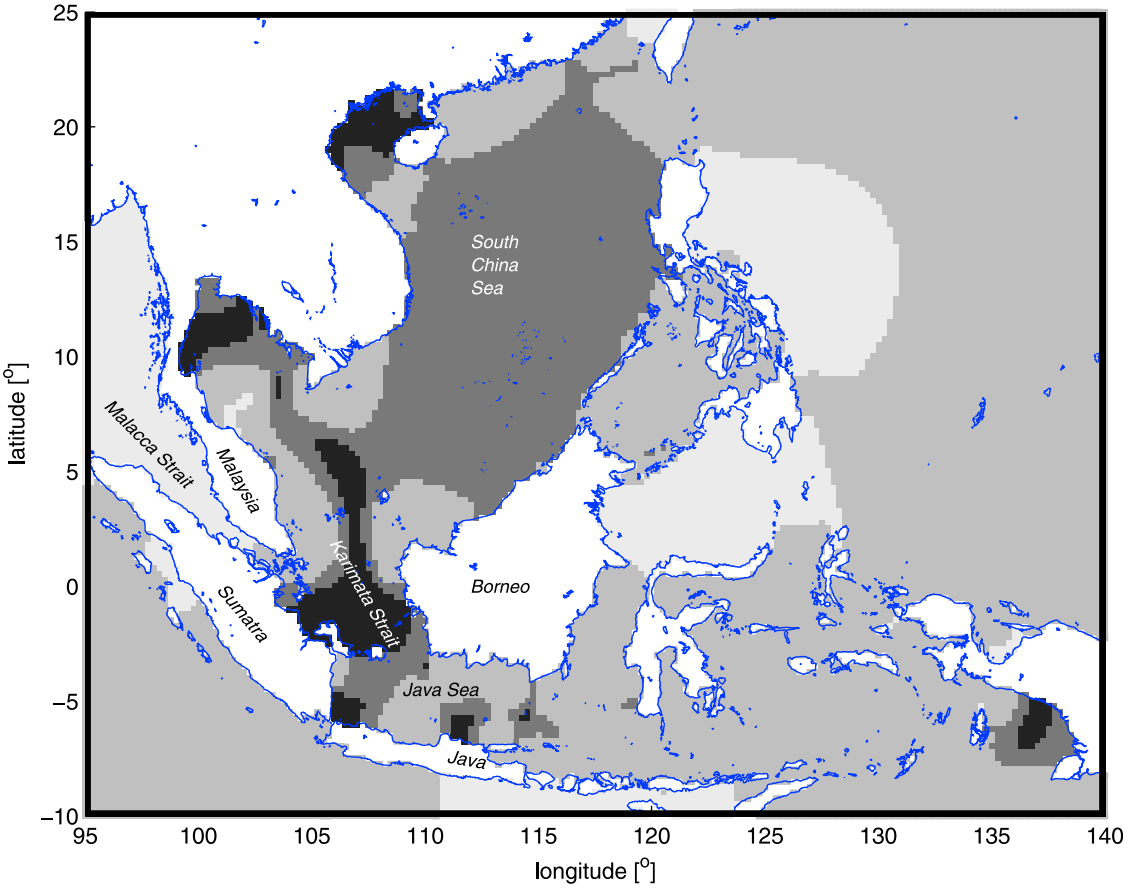

Figure 1. Tidal regimes in the South China Sea, based on constituent maps computed with the TPX06 ocean tide model (see *Egbert and Erofeeva* [2002] for the TPX model), using the tidal form factor F ($F = (A_{K1} + A_{O1})/(A_{M2} + A_{S2})$, where A is the tidal amplitude). Tides are diurnal for $F > 3$ (black) and semi-diurnal for $F < 0.25$ (light gray). The mixed tides in-between are dominantly semidiurnal for $F = 0.25$-1.5 and dominantly diurnal for $F = 1.5$-3.

oscillations associated with the moon's declination (K_1 and O_1). Their relative importance varies spatially due to local amplification and damping of the various constituents. Near Singapore, the tides are mixed, mainly semidiurnal. Singapore is located in an exceptionally sharp transition zone where the dominantly diurnal tides (in-between Sumatra and Borneo) change into semidiurnal tides (in-between Sumatra and Malaysia) within a distance of only 400 km (Figure 1 or *Hoitink* [2008]). The transition from diurnal to semidiurnal is the result of an increase of the M_2 amplitude (especially in the Singapore Strait) and a decrease in diurnal amplitudes [see *Zu et al.*, 2008]. Strong tidal currents occur where separate basins having different tidal regimes are connected by a narrow channel [e.g., *Pugh*, 1987]. Therefore, the sharp transition in tidal regimes is expected to generate strong tidal currents in the Singapore Strait. The low amplitude of the diurnal constituents is due to an amphidromic line from Borneo to the Malay Peninsula [see *Zu et al.*, 2008]. Near amphidromic points, water level oscillations are low while currents may be substantial. The opposite occurs near anti-amphidromic points, such as for the semidiurnal M_2 constituent close to Singapore [see *Zu et al.*, 2008]. As a result, water level oscillations are semidiurnal while flow velocity oscillations are diurnal [*Pugh*, 1987].

3. Modeling (Sub) Tidal and Residual Flow in the Singapore Straits

[11] Throughout this paper we distinguish between multiple timescales of flow asymmetry: residual flow, subtidal flow, tidal asymmetry, and residual transport. Residual flow is the long-term (here: yearly) averaged flow velocity. Subtidal flow is an oscillating flow component at frequencies lower than that of the diurnal tides, and may be tide or Monsoon driven. The seasonally varying Monsoon current is therefore not considered residual flow, but subtidal flow. Tidal asymmetry is a persistent, tide-generated difference in ebb and flood velocities, which can manifest itself in different maximum flow velocities (and consequently different durations of ebb and flood) but can also have the form of a difference in slack tide duration (with equal ebb and flood velocities). Tidal asymmetry is specifically generated by tidal constituents with frequencies at multiples of each other; the type of asymmetry is determined by the difference in tidal phases of the tidal constituents. Asymmetries caused by

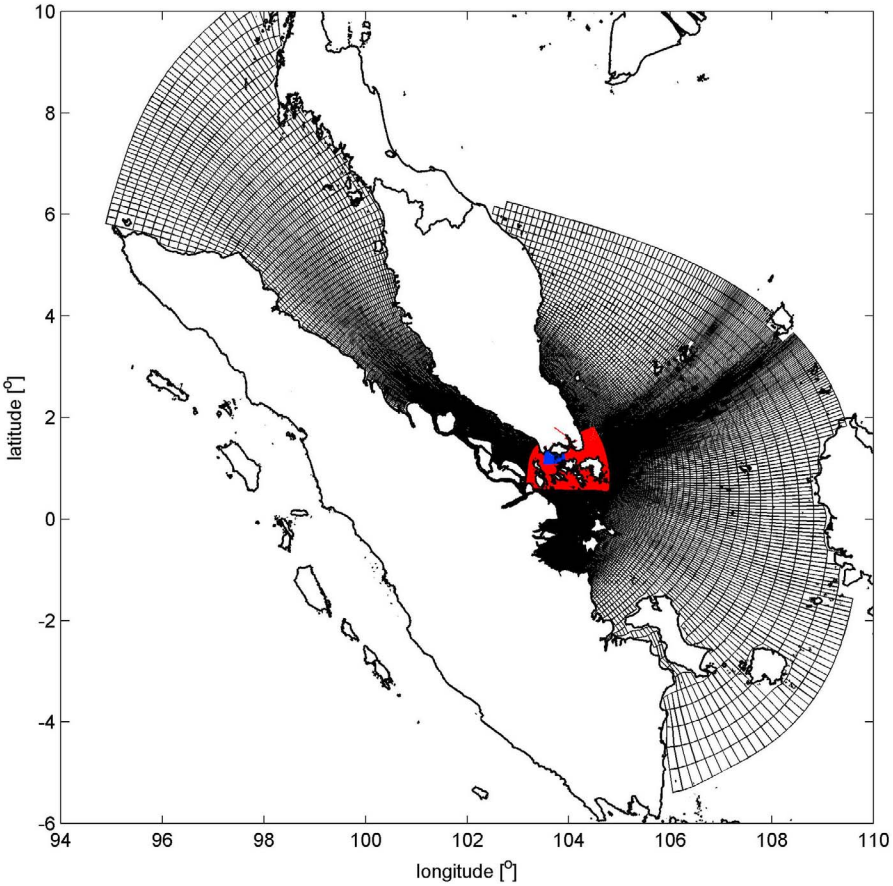

Figure 2. Curvilinear orthogonal boundary fitted model grids: the outer domain (black), the middle domain (red) and the inner domain (blue).

constituents with frequencies which are not exact multiples vary through time and disappear when averaged over sufficiently long timescales. Finally, residual transport of sediment may occur when there is an asymmetry in the flow velocity, either by residual flow or tidal asymmetry.

3.1. Model Description

[12] The (sub) tidal and residual flow is modeled using Delft3D-flow, simulating the shallow water equations, the continuity equations and the transport equations for conservative constituents. The set of partial differential equations in combination with appropriate initial and boundary conditions are solved with an Alternating Direction Implicit (ADI) finite difference scheme [*Stelling*, 1984; *Stelling and Leendertse*, 1992] on an Arakawa C grid [*Arakawa and Lamb*, 1977]. In the present study, baroclinic processes are negligible since the largest river draining into the Singapore Strait (the Johor River) has a yearly averaged discharge less than 80 m^3/s, and therefore the flow is modeled in depth-averaged mode. The model's efficient flexible orthogonal mesh features grid cell sizes that are ~30 km near the boundaries and gradually reduce to ~200 m around Singapore, which are further refined with a factor three through domain decomposition (Figure 2). The model is forced at its three open boundaries (the Andaman Sea in the northwest, the South China Sea in the northeast, and the Java Sea in the southeast by 8 tidal constituents (Q_1, O_1, P_1, K_1, N_2, S_2, M_2, and K_2) and a mean annual cycle of the Monsoon-induced water level, derived from 15 years of Topex-Poseidon (T/P) and Jason-1 satellite altimetry: see *Gerritsen et al.* [2009] and *Ooi et al.* [2009]. This monsoon-induced water level setup represents the effect of the large-scale wind patterns, and therefore wind is not explicitly modeled. Short-term (i.e., days) wind-driven events are therefore not accounted for.

[13] A constant discharge is prescribed for the Johor River and various smaller distributaries, with the total discharge flowing from the Johor River around 80 m^3/s. The boundary conditions were successively improved by *Ooi et al.* [2010] and *Kurniawan et al.* [2011] to better reproduce the tidal propagation in the Andaman Sea (Malacca Strait) and the South China Sea. Their model application was refined locally in the eastern part of Singapore and validated against flow velocity measurements in the Johor Estuary [see *Hasan et al.*, 2012]. The tidal dynamics in the Johor Estuary strongly differ from those in the Singapore Strait, where velocities have only been measured in the topographically complex Southern Island region. In order to reproduce the complex flows in this area, Hasan's model was refined locally with a factor 3 (see Figure 3), allowing accurate reproduction of the complex tidal flows through the islands.

[14] All simulations cover the period 1 January to 31 December 2004. Four water level stations and 2 flow velocity stations were used to compare model results with observations: see Figure 3. These stations were selected to

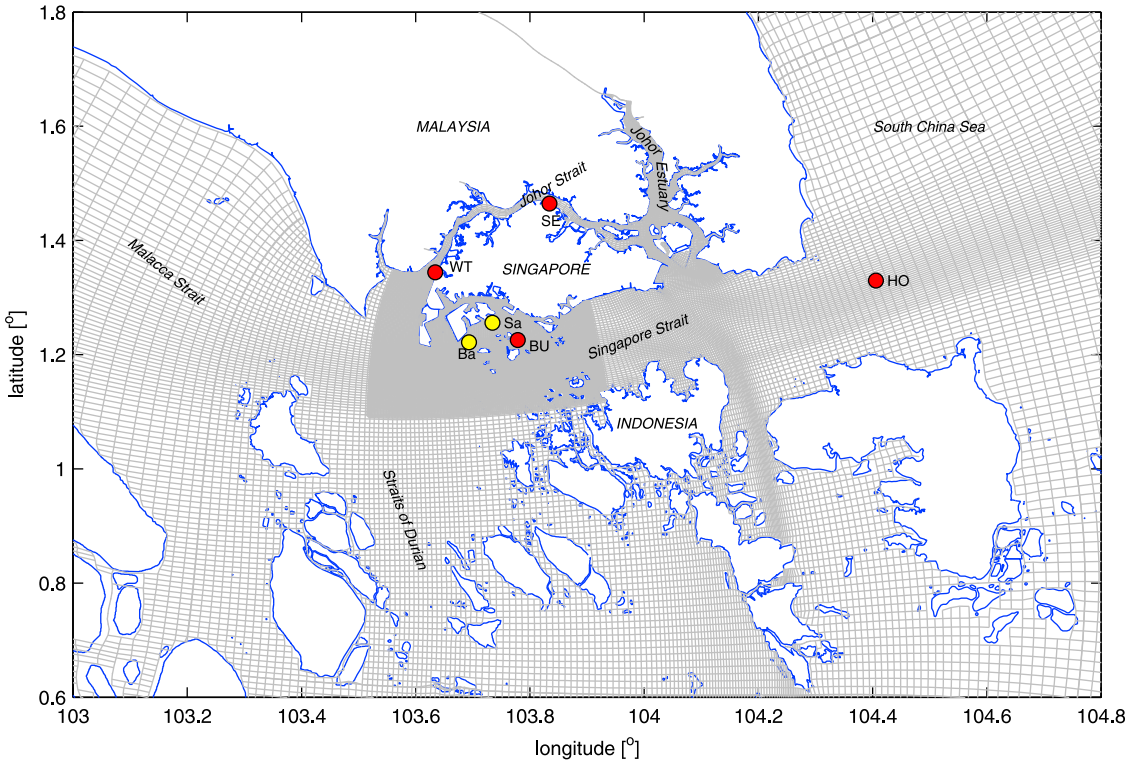

Figure 3. Map of the southern tip of the Malay peninsula, the Indonesian Riau islands, Singapore and the most important waterways: the Malacca and the Straits of Durian connected to the South China Sea through the Singapore Strait. The Johor Estuary and the Johor Strait separate Singapore from the Malay peninsula. The computational grid is shown in gray shades: the local grid Southwest of Singapore is 3 times refined. The locations of tide gauges are marked red: Horsburgh (HO), Sembawang (SE), Bukom (BU), and West Tuas (WT); the locations flow velocity measurements are marked yellow: Sawa Buoy (Sa) and Banyan Buoy (Ba).

cover a wide spatial scale, and have synchronous and reliable data. This latter criterion especially applies to the flow velocity stations: flow velocity measurements have been done at irregular time periods, and may have large periods of unreliable data. Even more, some stations were close to large-scale reclamations which strongly influence the flow patterns, but for which the exact bathymetry during the measurements was unknown. We only use near-surface measurements because observations at greater depth often appear to be unreliable [*Cronin and van Maren*, 2011].

[15] Both modeled and observed water levels and velocities are analyzed for 68 harmonic constituents by performing a classical harmonic analysis with nodal corrections, using the MATLAB version of T-Tide [*Pawlowicz et al.*, 2002]. The velocities are first harmonically analyzed in x and y direction using harmonic analysis, similar to that for water levels. These amplitudes and phases in the x and y direction were transformed into tidal ellipses to determine the amplitude and phase of the major axis of the tidal flow [*Xu*, 2000]. The constituents in the tidal analysis include S_A and S_{SA}.

[16] The effect of the Monsoons in the flow modeling, realized through the T/P based mean annual cycle, results in contributions that include frequencies equal or close to S_A and S_{SA}. For Singapore waters, periodic behavior with frequencies corresponding to that of S_A and S_{SA} will be primarily generated by the large-scale pressure variations (driving the Monsoons in the South China Sea), and are not the S_A and S_{SA} constituents generated by the Earth-moon system in the Equilibrium Tide. Additionally, M_{SF}, and M_F are constituents in the equilibrium tide, but their frequencies are equal to compound tides generated by O_1, K_1, M_2, and S_2. The frequencies of these 4 constituents are based on 3 basic constituents: ω_1, ω_2, and ω_3 (frequencies of 14.49205, 0.54902, and 0.04109 °/h, resp.). With ω expressed in °/h, the synodic period (in days) for two frequencies to overlap is $T_{ab} = 360/(\varpi_a - \varpi_b)/24$. The synodic period of different constituents can then be computed from their basic frequencies (Table 1). Additionally, compound tides are generated by interaction of the 4 main harmonic constituents. The different interactions have three important implications, which will be discussed below.

[17] M_2 and S_2 generate the MS_0 compound tide (with a period equal to the duration of the M_2 and S_2 spring-neap tidal cycle) whereas O_1 and K_1 generate the KO_0 compound tide (with a period equal to the duration of the O_1 and K_1 spring-neap tidal cycle). The frequency of MS_0 and KO_0 equals that of M_{SF} and M_F (resp.): constituents in the equilibrium tide known to be exceptionally large in the South China Sea [see *Egbert and Ray*, 2003]. Since M_{SF} and M_F are not prescribed at the model boundaries, all modeled energy in the M_{SF} and M_F bands is strictly MS_0 and KO_0 (resp.). Second, M_2 shares its frequency with the constituent KO_2, which is the sum of the frequencies of O_1 and K_1. In most semidiurnal and mixed tidal regimes, the amplitude of

Table 1. Frequencies and Periods of O_1, K_1, M_2, S_2 and Synodic Periods

Equilibrium Tide	Combination	Compound Tide	Basic Frequencies	T
O_1			$\omega_1 - \omega_2$	25.819 hours
K_1			$\omega_1 + \omega_2$	23.934 hours
M_2	(O_1+K_1)	KO_2	$2\ \omega_1$	12.421 hours
S_2			$2\ \omega_1 + 2\ \omega_2 - 2\ \omega_3$	12.000 hours
M_F	(O_1-K_1)	KO_0	$2\ \omega_2$	13.661 days
M_{SF}	(M_2-S_2)	MS_0	$2\ \omega_2 - 2\ \omega_3$	14.765 days
S_{SA}	(O_1-K_1)-(M_2-S_2)		$2\ \omega_3$	182.62 days

M_2 will be much larger than KO_2. However, in diurnal regimes, part of the energy in the M_2 frequency may actually stem from the frequencies of the O_1 and K_1 constituents. Since the frequency is identical, this cannot be discerned through standard harmonic analysis. Since the phases of M_2 and KO_2 are usually different, KO_2 may strengthen or weaken the M_2 tidal signal. Third, spring tides are highest when O_1-K_1 spring tide overlaps with M_2-S_2 spring tide. This happens exactly two times per mean tropical year (365.2422 days): see Table 1. This implies that the highest spring tides always occur during the same period of the year, and therefore always occurs in the same Monsoon period.

3.2. Water Levels

[18] The harmonic fit to the modeled water levels typically explains more than 99.4% of the variance while between 98.8 and 99% of the variance in observed water levels is explained. The subtidal frequencies (S_A to KO_0) are less accurately reproduced by the model than the tidal frequencies (Table 2). The observed westward amplitude decrease (from Horsburgh to West Tuas) of S_A (from 13 to 2 cm) and increase of S_{SA} (from 3 to 5 cm) is qualitatively reproduced by the model, although with lower spatial gradients (S_A decreasing from 10 to 5 cm, and S_{SA} increasing from 2 to 4 cm). The phases of the observed S_{SA} and S_A constituents are spatially more variable than the model, and modeled phases may deviate up to 50° from observed phases. However, since these constituents represent Monsoonal variations which should vary synchronously over such small spatial scales, it seems that the observed phase differences may be less reliable than the modeled phases. Of the tabulated diurnal constituents, the amplitude of O_1 is often slightly underestimated while the amplitude of K_1 is slightly overestimated. The modeled average amplitude of O_1 and K_1 (representing the main diurnal signal), approximates the observed average amplitude of O_1 and K_1 within 1–2 cm. The amplitude of the diurnal constituents slightly decreases in the westward direction. The observed amplitude of the semidiurnal constituents strongly increase in the westward direction: from 57 cm to 94 cm (M_2) and from 19 to 43 cm (S_2). The modeled amplitudes of both semidiurnal constituents approximate observations within 4 cm (see Table 2). The tidal waves of all constituents propagate in the westward direction, with modeled phases typically within 10 to 20° of observations. The amplitude of M_4 (the main overtide in most coastal systems) is low. The observed westward increase in M_4 from 1 to 6 cm is reasonably captured by the model.

3.3. Flow Velocities

[19] Comparison between observed and computed flow velocities is less straightforward in general, but near Singapore in particular. First, flow velocity is a vector, composed of magnitude and direction. Second, flow velocities are more strongly influenced by nontidal processes such as local winds, introducing nontidal energy at tidal frequencies [e.g., see *Pugh*, 1987], and are more sensitive to changes in depth and to influences of embayments, headlands, and islands. Third, in Singapore waters, flow velocity measurements are available for 2002, 2003, and 2005 onward, but not for 2004, the year that is modeled for reasons of showing the strongest nontidal features. Finally, these flow velocity measurements in Singapore have frequently been carried out to monitor effects of large-scale marine construction works (i.e., land reclamation), and therefore their direction and magnitude may change during the period of observation. Nevertheless, tidal velocities can be analyzed in the same way as water levels as long as results are carefully interpreted. The most accurate and continuously and available flow velocity data sets (measured in 2003) are shown in Figure 4. Flow velocities are highest around June and lowest in September–October, with stronger eastward currents than westward currents. The low-passed flow velocities (using a

Table 2. Observed and Modeled Water Level Amplitude A and Phase ϕ, at Horsburgh, Sembawang, Bukom, and West Tuas[a]

	Horsburgh				Sembawang				Bukom				West Tuas			
	A (cm)		ϕ (°)		A (cm)		ϕ (°)		A (cm)		ϕ (°)		A (cm)		ϕ (°)	
Const	O	M	O	M	O	M	O	M	O	M	O	M	O	M	O	M
S_A	13	10	353	346	14	9	9	340	7	7	343	337	2	5	279	328
S_{SA}	3	2	98	150	4	3	48	148	4	3	126	153	5	4	121	157
MS_0	1	0	93	80	4	2	14	52	3	2	70	53	5	4	60	47
KO_0	3	1	30	50	6	0	2	267	3	1	19	7	3	1	6	289
Q_1	5	7	355	316	5	5	14	60	4	5	33	57	3	5	62	82
O_1	29	27	28	24	29	23	48	57	25	22	77	90	25	23	112	117
P_1	10	10	71	46	11	8	97	211	8	8	122	117	8	10	152	140
K_1	29	33	76	67	31	28	100	104	27	29	131	139	27	33	160	158
N_2	12	9	279	283	17	15	303	320	16	15	310	319	18	17	318	322
M_2	57	55	308	310	84	81	325	341	82	81	329	349	94	90	333	353
S_2	19	18	7	17	32	33	27	46	35	35	24	47	43	41	27	46
K_2	6	5	3	8	9	10	29	40	10	10	21	42	13	12	23	38
M_4	1	1	59	72	5	4	45	31	3	6	274	319	6	8	254	302

[a]Observed is O and Modeled is M.

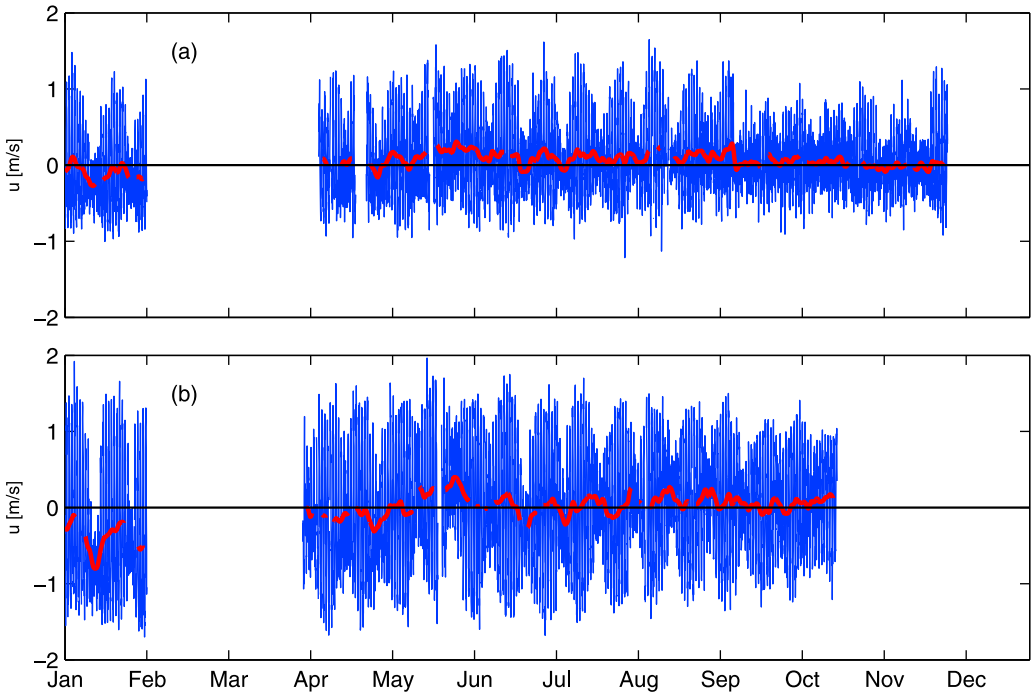

Figure 4. Measured surface flow velocity at (a) Sawa Buoy, and (b) Banyan Buoy in the main flow direction (eastward positive, in m/s), in 2003. The red line is the low-frequency flow velocity obtained by applying a Godin filter, removing all signals in the semidiurnal and diurnal frequency bands [*Godin*, 1972]. Data is from the Maritime Port Authorities (MPA).

Godin filter; *Godin* [1972]) show a seasonal variation with eastward flow in June and westward flow in January, with superimposed oscillations at frequencies of the spring-neap cycles. These patterns will be explained in a following section; first the data is applied to validate the model.

[20] Table 3 shows that the flow velocities at higher frequencies (diurnal to quarter-diurnal) are overestimated, while the low-frequency components (S_A and S_{SA}) are underestimated. This discrepancy may be the result of local effects, of large-scale tidal behavior, or of a more than average Monsoon effect in 2004. Local bathymetric effects may lead to local increase of flow velocities, which are often difficult to exactly reproduce using a numerical model in a large area with a highly variable topography and bathymetry, such as the Singapore Strait. As a result, in the comparison of measured and observed currents the spatial representativity of the data needs to be included. The spatial variation in the current amplitude is very high (as will be discussed in section 3.4), which means that a small spatial error in the velocity (resulting from, e.g., an incorrect bathymetry) may lead to large (but local) errors in the flow velocity amplitude. The model overestimates the current amplitudes of all the diurnal to quarter-diurnal constituents while the phasing is in good agreement with observations, suggesting local effects do indeed cause the overestimated current amplitudes. The phases of all constituents, with the exception of M_4, are well reproduced. Despite possible spatial effects mentioned above, it appears that the M_2 current amplitude is overestimated more strongly than all other constituents.

[21] In order to compare the actual observations with the harmonic estimates of the model results and the observations, the harmonic constituents are expanded into time series for one spring-neap cycle (using residuals and all constituents) and 1 year (using residuals and low-frequency constituents). The spring-neap comparison (Figure 5) shows that the harmonic estimates of the modeled and the data-derived constituents agree fairly well: the pronounced asymmetry in the flow (with the spring eastward flow velocity typically 0.5 m/s larger than the westward flow velocity) is reproduced. The harmonic fit to the flow velocity observations agrees better with the modeled harmonic prediction than with the actual observations. This suggests that

Table 3. Observed and Modeled Major Axis of the Tidal Ellipse and phase ϕ, at Sawa Buoy and Banyan Buoy[a]

	Sawa Buoy				Banyan Buoy			
	U_{major} (cm/s)		ϕ (°)		U_{major} (cm/s)		ϕ (°)	
Const	O	M	O	M	O	M	O	M
S_A	14	7	195	184	20	9	206	183
S_{SA}	2	1	154	167	7	2	102	125
MS_0	4	4	60	53	6	5	68	57
KO_0	3	4	263	242	2	3	348	248
Q_1	4	8	186	191	8	11	195	190
O_1	28	36	205	218	51	51	214	215
P_1	14	13	245	234	10	18	227	231
K_1	28	44	262	258	49	62	262	255
N_2	4	5	70	67	5	6	72	60
M_2	12	28	78	109	19	36	71	105
S_2	7	11	85	126	14	15	82	118
K_2	1	3	279	16	3	3	321	19
M_4	1	2	279	16	3	3	321	19

[a]Observed is O and Modeled is M. Tidal Ellipse is in cm/s.

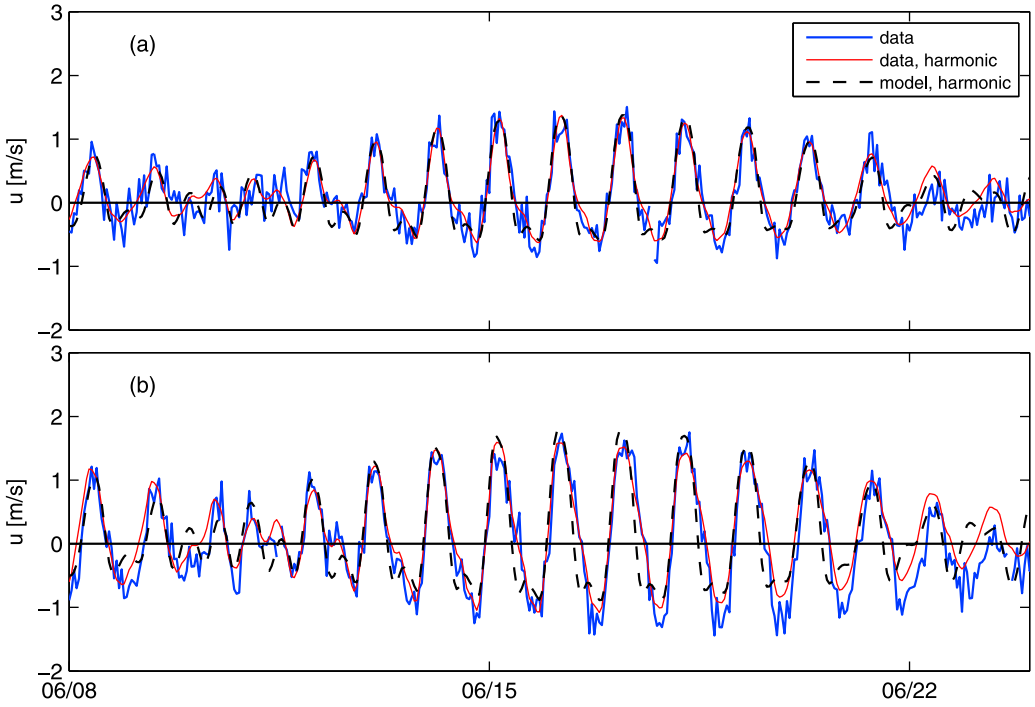

Figure 5. Measured surface flow velocity (thick blue line), harmonic fit to the measured surface flow velocity (red line), and harmonic extrapolation to 2003 of the modeled depth-averaged flow in 2004 (black line), at (a) Sawa Buoy and (b) Banyan Buoy. The measured and computed flow velocities are in the main flow direction, in m/s, with eastward positive.

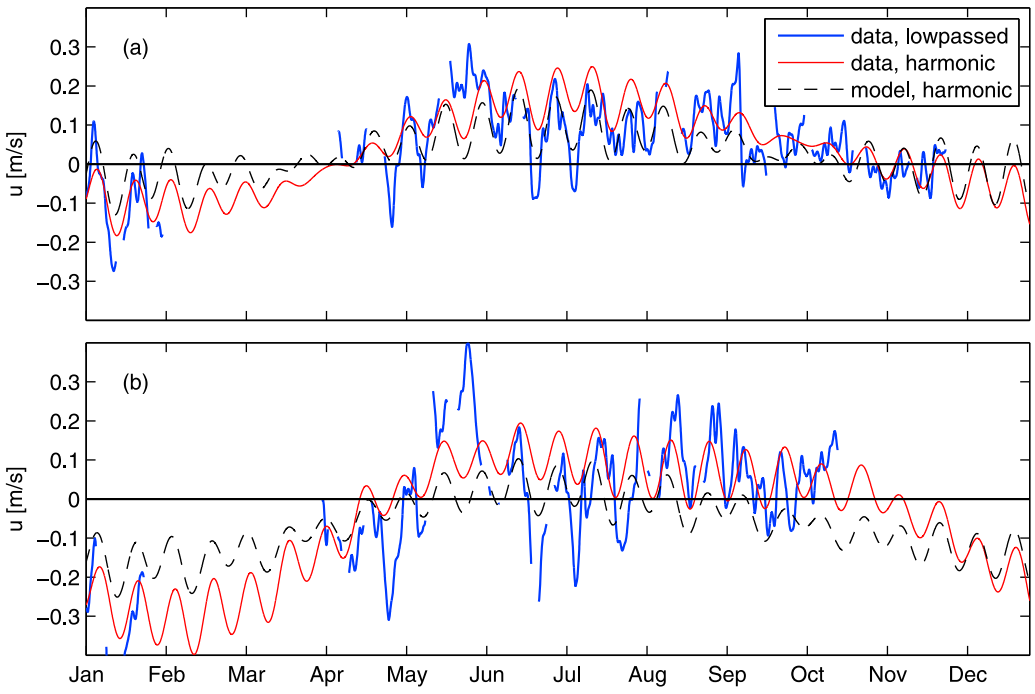

Figure 6. Subtidal and residual flow velocity (m/s, eastward positive): low-passed observed flow velocity (using a Godin filter; thick blue line) and harmonic fits to observations (red) and model (dashed black line), at (a) Sawa Buoy and (b) Banyan Buoy. Harmonic estimates are based on residual flow and the low-frequency constituents: S_A (annual), S_{SA} (semiannual), M_{SM} (solar monthly), M_M (lunar monthly), MS_0 (solar semimonthly), and KO_0 (lunar semimonthly).

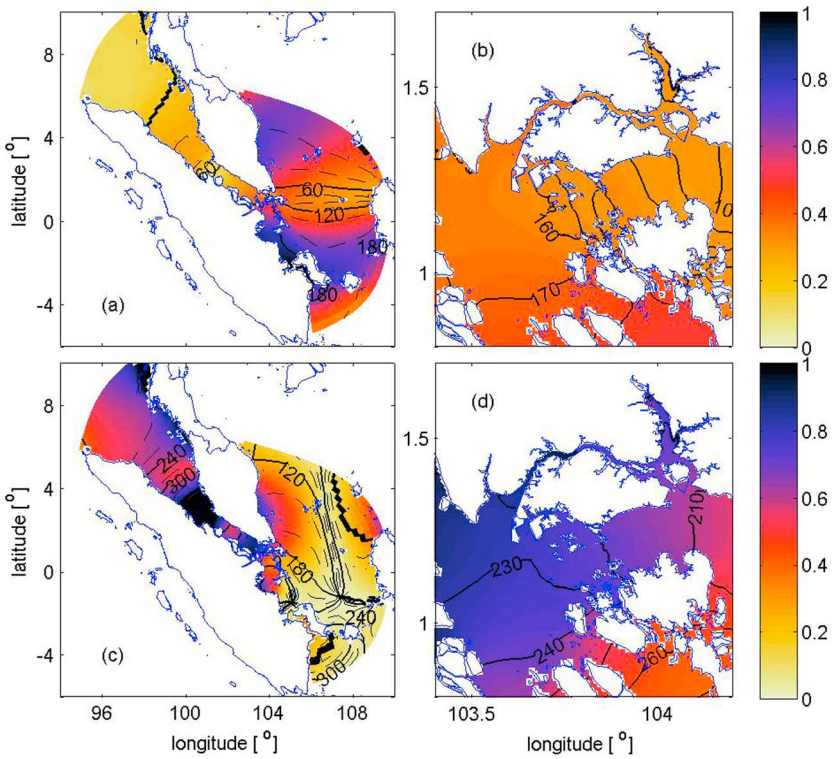

Figure 7. Water level phase in (a and c) the entire model domain (with solid lines at 60° intervals, dashed lines at 20° intervals) and (b and d) detail near Singapore (solid lines every 10° interval), as well as amplitude of K_1 (Figures 7a and 7b) and M_2 (Figures 7c and 7d) in isocolors.

the difference between observations and harmonic estimates is primarily related to shorter term nontidal (probably wind-driven) effects. More importantly, the agreement between the harmonic fit to observations and model implies that the tidal motions in Singapore's coastal waters are well reproduced. The full year comparison (Figure 6) shows that the magnitude of the model underestimates the half-yearly and yearly flow velocity components at Banyan Buoy (resulting in westward currents being too weak during the SW Monsoon), although the phasing is reasonable: the modeled Monsoon-induced flow reversal differs only several days to weeks from observations. It should be noted that there is little data available for Banyan Buoy in the SW Monsoon, where the model differs most from the harmonic fit to the observations. Superimposed on these yearly and half-yearly variations are the monthly and the half-monthly constituents, which appear to agree fairly well in terms of phasing and amplitude. Similar to the spring-neap comparison, the harmonic estimates to the flow velocities agree better with the harmonic estimates of the modeled flow velocities than to the actual (low-passed filtered) velocity data.

3.4. Tidal Dynamics

[22] The diurnal tides primarily originate from the South China Sea. The diurnal K_1 tide propagates from the South China Sea and the Java Sea into the Karimata Strait, where it reflects against the eastern coast of Sumatra (Figure 7). The reflection against the Sumatran coast results in strong amplification of the amplitude of the diurnal components, with values close to 1 m for O_1 and K_1. A third wave enters from the Andaman Sea, although of much lower amplitude. The phase and amplitude of the K_1 tidal wave suggests it to be a standing wave with antinodes west of the Malay Peninsula and the Sumatran Coast, and with a node close to Singapore. In a standing wave, flow velocities are low near anti-nodes and maximal near nodes. The area with low diurnal water level amplitudes, stretching from Singapore Eastward to Borneo, has much higher diurnal flow velocity amplitudes than elsewhere (not shown here). This standing wave pattern therefore explains the high flow velocities of the diurnal constituents close to Singapore (Figure 8). The strong tidal currents that exist in the Singapore Strait are primarily connected to the Durian Straits, while tidal exchange of K_1 with the Malacca Strait is limited (Figure 8).

[23] The M_2 tidal wave behaves as a Kelvin wave rotating in the anticlockwise direction around an amphidromic point located halfway Borneo and Sumatra, in the Karimata Strait (see Figure 7). The main M_2 tidal wave enters from the Andaman Sea through the Malacca Strait. The flow through the Malacca Strait diverges into the Durian Straits and into the Singapore Strait, with highest flow velocities occurring in the Durian Straits (Figure 8).

[24] A more detailed analysis of the tidal flows in Singapore's waters reveals a pronounced difference in the relative importance of diurnal and semidiurnal currents. The tidal form factor shows that water levels and currents in the South China Sea (East of Singapore) are diurnal while water levels and currents in the Malacca Strait (West of Singapore) are semidiurnal (Figure 9). Closer to Singapore, the water levels are semidiurnal in the west of Singapore's waters ($F \approx 0.25$) but become mixed, semidiurnal ($F \approx 0.5 - 1$) in the east. In contrast, the form factor of the current velocities indicates

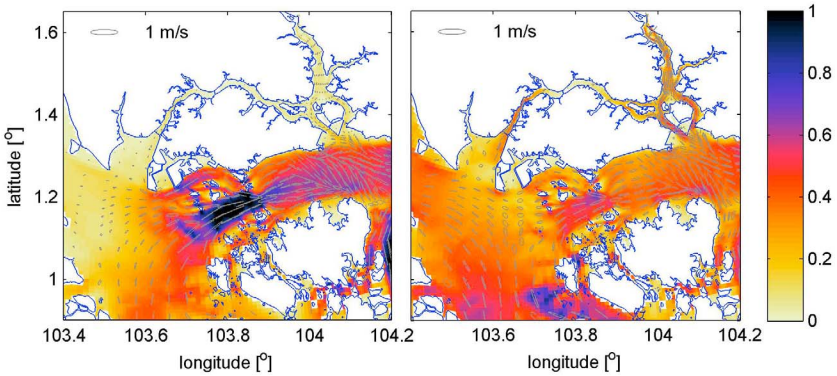

Figure 8. Velocity amplitudes and tidal ellipses of (left) K_1 and (right) M_2.

that the currents in the Singapore Strait are mainly mixed, dominantly diurnal ($F = 1.5–3$) but locally even diurnal ($F > 3$). This clearly demonstrates that the currents in the Singapore Strait are driven by tidal oscillations further away. The diurnal currents are strong because the diurnal tidal waves propagating through the Singapore Strait amplify as they reflect against the Sumatran coast. Diurnal water levels are low because of the nearby diurnal amphidromic line from the tip of the Malay peninsula to Borneo. The water bodies in which the flow is strongly affected by local geometry and bathymetry variations (such as the Johor Estuary and the Johor Strait) have semidiurnal flow velocities. It is also noteworthy that various causeways constructed to connect Singapore with Malaysia and its islands have in some areas led to a transition from dominantly diurnal flow (as part of large-scale flow patterns) to dominantly semidiurnal flow (driven by local water level variations).

[25] In a mixed tidal regime, the spring-neap tidal cycles of the 2 main diurnal constituents (O_1 and K_1) and the spring-neap variation of the main semidiurnal constituents (M_2 and S_2) overlap 2 times per year (resulting in a frequency of $2\varpi_3$, see Table 1). The period coinciding with

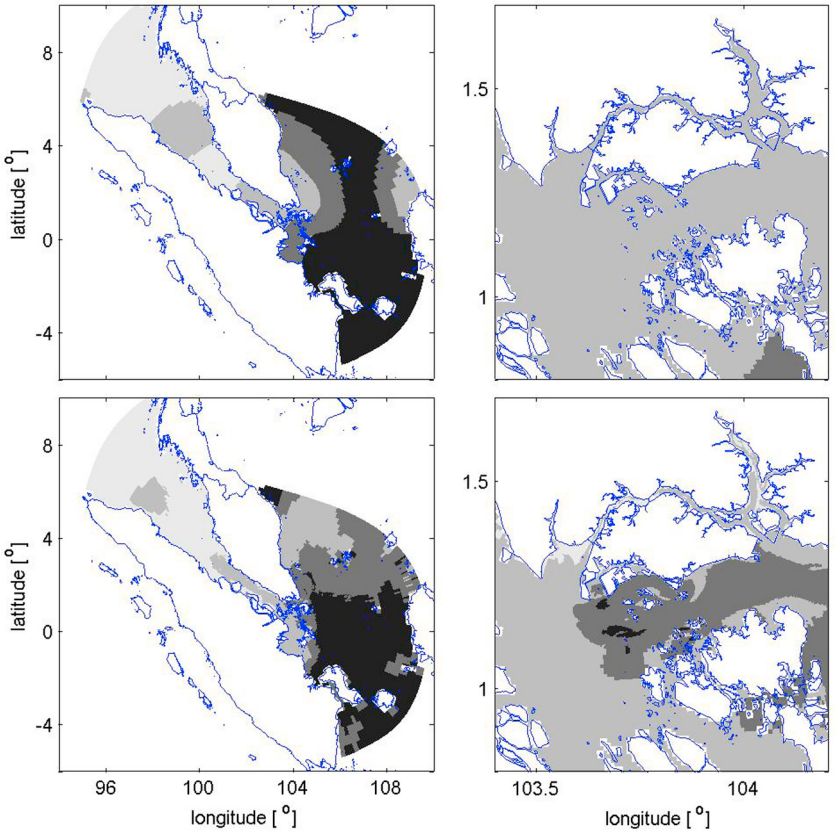

Figure 9. Tidal regime, based on the tidal form factor F ($F = (A_{K1} + A_{O1})/(A_{M2} + A_{S2})$) for (top) water levels and (bottom) currents in (left) the whole model domain and (right) in detail near Singapore. Black is diurnal ($F > 3$), light gray is semidiurnal ($F < 0.25$), greyshades in-between are mixed, dominantly semidiurnal ($F = 0.25–1.5$) to diurnal (1.5-3).

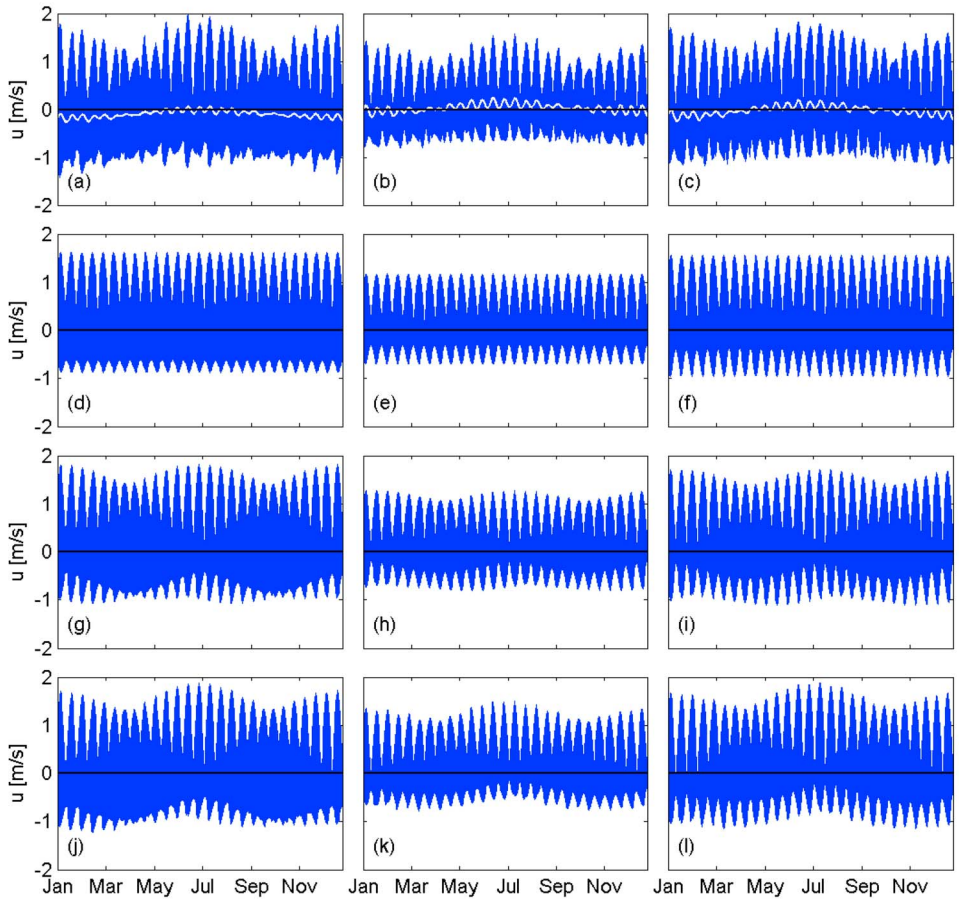

Figure 10. Flow velocity (m/s, eastward positive) based on harmonic analysis of modeled flow velocities at (a, d, g, j) Horsburgh, (b, e, h, k) Sawa Buoy, and (c, f, i, l) Banyan Buoy. Harmonic expansion of all constituents (blue) and only the low-frequency constituents SA, SSA, M_{SM}, M_M, MS_0, KO_0 and the residual (white) are given in Figures 10a–10c. The harmonic expansion of O_1, K_1, and M_2 is shown in Figures 10d–10f, while the harmonic expansion of O_1, K_1, M_2 and S_2 is shown in Figures 10g and 10h. Figures 10j–10l show the harmonic expansion of the residual flow, the low-frequency constituents SA, SSA, M_{SM}, M_M, MS_0, KO_0 and the dominant constituents O_1, K_1, M_2 and S_2.

$2\varpi_3$ is exactly a half year, which implies that the highest spring tides always occur during the same period of the year, and does not shift through time. A full year of modeled time series at three locations reveals that maximum current velocities occur in June and December (Figures 10a–10c), when semidiurnal spring tides occurs simultaneously with diurnal spring tides.

[26] The asymmetry of the tides results from the inclination of O_1, K_1, and M_2 (see Figures 10d–10f). Table 1 reveals that the frequency of O_1 and K_1 combined is equal to that of M_2. This implies that the inclination of M_2 with the diurnal spring-neap cycle is persistent in time. This was elaborated by *Hoitink et al.* [2003], showing that a constant phase angle relationship defined as $\theta = \cos(\phi_{u(O_1)} + \phi_{u(K_1)} - \phi_{u(M_2)})$ exists, where ϕ_u is the phase of the individual constituent. This is similar to the constant phase inclination of M_2 with its overtide M_4, $\theta = \cos(2\phi_{u(M_2)} - \phi_{u(M_4)})$, which dominates tide-induced net transport rates in many shallow coastal systems, e.g., see *Aubrey* [1986], *Friedrichs and Aubrey* [1988], and *Wang et al.* [2002]. Flow velocities are symmetric for $\theta = 0$, and maximally asymmetric for $\theta = 1$ or -1. For morphological changes in diurnal or mixed tidal regimes, the phase inclination of O_1, K_1, and M_2 may be equally important as $M_2 - M_4$, or probably even more important [*van Maren et al.*, 2004].

[27] Throughout the Singapore Strait, flow velocities are asymmetric with higher eastward flow velocities than westward flow velocities (Figures 10a–10c). This asymmetry is reasonably reproduced with only O_1, K_1, and M_2 (Figures 10d–10f). The modeled phase inclination $\theta = \cos(\phi_{u(O_1)} + \phi_{u(K_1)} - \phi_{u(M_2)})$ typically is close to 1 (see Table 3) which implies that tidal asymmetry due to the O_1-K_1-M_2 triad is near its maximum. For maximum asymmetry, the difference between ebb and flood then is twice the velocity amplitude of M_2, creating a typical difference between ebb and flood of 0.5 m/s (see Table 3). This agrees fairly well with the asymmetry in Figures 10a–10c. However, the semiannual cycle in the tidal current amplitude (and therefore also the degree of asymmetry) requires the S_2 constituent (Figures 10g–10i). Although these 4 constituents reasonably reproduce the semiannual cycle in spring tidal current amplitude resulting from all constituents

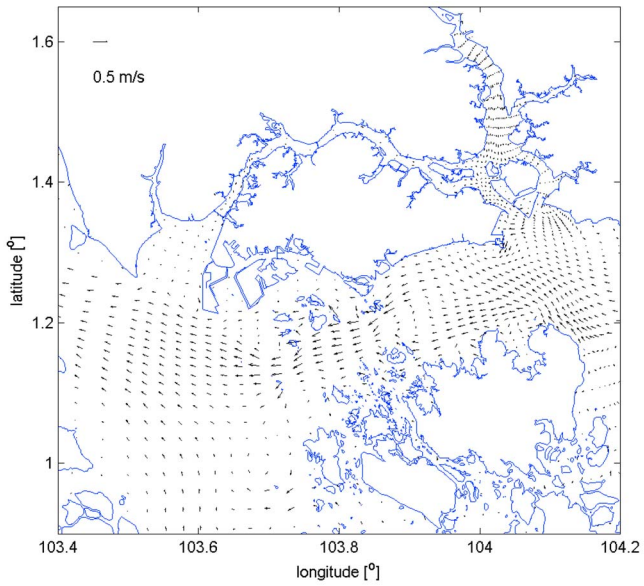

Figure 11. Eulerian residual flows (vectors in the refined domain coarsened three times) averaged over 365 days.

(Figures 10a–10c), the semiannual modulation of the spring tides is still underestimated. This requires additional subtidal components (the (half) yearly as well as fortnightly constituents): see Figures 10j–10l. The yearly (monsoon) cycle influences the degree of asymmetry, with stronger eastward flow in June (and hence stronger asymmetry) and weaker eastward flow in December (and therefore weaker asymmetry). The fortnightly constituents influence the spring tidal amplitudes: KO_0 and MS_0 are, respectively, in phase with O_1-K_1 and M_2-S_2 (June and December).

3.5. Subtidal and Residual Flows

[28] Subtidal flows may be driven by density gradients, wind stress or by higher frequency tides. Here we ignore the baroclinic density gradients, but focus on the barotropic tidal and meteorological effects. As explained in section 3.1, the fortnightly constituents have an astronomical and a friction-induced component. Our model only simulates friction-induced fortnightly constituents (the compound tides MS_0 and KO_0). The good agreement with observed fortnightly constituents (Figure 6) strongly suggests that the fortnightly constituents around Singapore are primarily originating from the interaction of O_1-K_1 and M_2-S_2, and not from astronomical forcing. This is in line with findings by *Egbert and Ray* [2003], who concluded that the amplitude of the fortnightly constituents in the South China Sea are 2–4 times higher than those in the equilibrium tide. From our model results we observe that these large fortnightly constituents are probably friction-induced, and not of astronomical origin.

[29] Meteorological effects generate local wind- or storm driven currents, the Monsoon-driven oscillating currents, but also a persistent westward flow. Storm-driven currents typically last for several days, and are unpredictable (at least on the long-term); these are beyond the scope of this study. The Monsoon-driven currents have a return interval of 1 year and are fairly predictable. The persistent westward flow is generated by the water level gradient between the Andaman Sea and the South China Sea [*Wyrtki*, 1961], which are indirectly related to the Monsoon winds.

[30] Persistent residual Eulerian flow velocities (as simulated with our model) of tidal origin are attributed generation of vorticity [*Zimmerman*, 1978]. Lagrangean flow velocities additionally contain a Stokes drift component [e.g., *Tarya et al.*, 2010]. The Stokes drift generates an additional residual term in case of progressive tidal waves [*Longuet-Higgins*, 1953]. However, the flow velocities are mainly diurnal while the diurnal water level amplitudes are fairly low, especially compared to the water depth (50 to 100 m in the Singapore Strait), and therefore the Stokes drift is probably insignificant compared to the Eulerian residual flow. This then implies that the Eulerian flow velocity corresponds to the Lagrangean flow velocity.

[31] Modeled residual flow velocities are visualized in Figure 11. These residuals are the average Eulerian currents based on 1 year of hourly computed flow velocity, per grid cell. A net westward residual flow exists at flow velocities over several dm/s. The flow velocities are highest in the Singapore Strait just south of the Southern Islands. Note that residual flow velocities in the area for which observations exist (see Figure 3) are substantially lower than further south in the Singapore Strait. Superimposed on these persistent residual flows are low-frequency tidal currents, which may occasionally lead to a reverse in residual flow directions: see Figure 6. The modeled flow through the Singapore Strait equals 70.7 10^3 m/s, or 0.07 Sv. Although this flow connects the Atlantic with the Indian Ocean, and could therefore be considered as part of the Indonesian Throughflow, this volume transport is 2 orders of magnitude lower than that through the main Indonesian Straits (typically several Sv; see *Gordon* [2005]).

4. Residual Transport

[32] The analyses in section 3 reveal that a pronounced tidal asymmetry exist, with large diurnal tides, low M_2 velocities compared to the diurnal flow velocities, and much larger M_2 than S_2 velocities. For such conditions, the *Hoitink et al.* [2003] O_1-K_1-M_2 triad is a valuable tool to analyze transport patterns. In order to separate the contributions of residual flow and tidal asymmetry to net transport of sediment, we follow the approach of *van Maren et al.* [2004]. They assume the transport to adapt instantaneously to the flow, which is valid for coarse-grained bed material transport but not necessarily for fine-grained bed material load. This method therefore only provides a first-order estimate of transports. We will verify the computed analytical transports with a full sediment transport model. The residual sediment transport is computed by introducing a fine-grained (settling velocity 1 10^{-6} m/s), easily erodible (critical shear stress for erosion of 0.1 Pa), with a concentration of 5 mg/l at the model boundaries. Additionally, an unlimited amount of sand with a median grain size of 200 μm is prescribed at the bed, of which the sediment transport is computed using the *van Rijn* [1993] equations for suspended and bed load transport. The direction of sand transport is dictated by both residual flow and by tidal asymmetry.

[33] Assuming the transport to adapt instantaneously to the flow, sediment transport can be parameterized with a

relatively simple bed load transport formulation such as the transport formula developed by *Bagnold* [1966]. His expression reads:

$$q = \bar{u}^3 \frac{\rho}{(\rho_s - \rho)} \frac{e_b}{C^2 \tan\alpha}$$

Where q is the volumetric transport ($m^3/s/m$), e_b is a dimensionless efficiency factor (0.15 for fine sand), C the Chézy coefficient ($m^{1/2}s^{-1}$), ρ is the water density (kg/m^3), ρ_s the sediment density (kg/m^3), and tan α the angle of repose of sediment (0.6). We define a rectilinear velocity field composed of a residual flow component $\bar{u}_r$ and a flow velocity by the O_1, K_1, and M_2 constituents as

$$\begin{aligned}\bar{u}_t = \bar{u}_r &+ A_{u(O_1)} \cos\left(\varpi_{(O_1)} t - \phi_{u(O_1)}\right) \\ &+ A_{u(K_1)} \cos\left(\varpi_{(K_1)} t - \phi_{u(K_1)}\right) \\ &+ A_{u(M_2)} \cos\left(\varpi_{(M_2)} t - \phi_{u(M_2)}\right)\end{aligned}$$

Where A_u, ϕ_u, and ϖ are the velocity amplitude, phase, and angular speed of each constituent. The assumption of a rectilinear velocity field implies we ignore the semiminor axes of the tidal constituents, and assume alignment of the three tidal ellipses. This assumption is required for a relatively straightforward analytical solution, and justified by the tidal ellipses shown in Figure 8. Since $\varpi_{(M_2)} = \varpi_{(O_1)} + \varpi_{(K_1)}$, there is a periodicity in this equation which can be eliminated by integrating the cubed velocity over an infinite number of cycles:

$$\bar{u}^3 = \lim_{T\to\infty} \frac{1}{T} \int_0^T \bar{u}_t^3 dt = \bar{u}_r^3 + a\bar{u}_r + b$$

The $\bar{u}_r^3$ term represents transport by residual flows only and the $a\bar{u}_r$ term represents transport of sediment by residual flow and tidal stirring. Tidal stirring (a) is part of the residual flow term since residual flow generates residual transport if sediment is brought in suspension by a flow velocity other than the residual flow, which is generally too weak to resuspend sediments. Transport by tidal asymmetry is represented by b. The tidal stirring term a can be a scalar, whereas the tidal asymmetry term b is computed in x and y direction:

$$a = \frac{3}{2}\left(A_{u(O_1)}^2 + A_{u(K_1)}^2 + A_{u(M_2)}^2\right),$$

$$b_x = \frac{3}{2} A_{ux(O_1)} A_{ux(K_1)} A_{ux(M_2)} \cos\left(\phi_{ux(O_1)} + \phi_{ux(K_1)} - \phi_{ux(M_2)}\right)$$

$$b_y = \frac{3}{2} A_{uy(O_1)} A_{uy(K_1)} A_{uy(M_2)} \cos\left(\phi_{uy(O_1)} + \phi_{uy(K_1)} - \phi_{uy(M_2)}\right)$$

Sediment transport by tidal asymmetry q_{as} and residual flow q_{res} can then be defined as:

$$q_{as,x} = b_x \frac{e_b}{C^2(\rho_s - \rho)\tan\alpha}$$

$$q_{as,y} = b_y \frac{e_b}{C^2(\rho_s - \rho)\tan\alpha}$$

$$q_{res} = \left(\bar{u}_r^3 + a\bar{u}_r\right) \frac{e_b}{C^2(\rho_s - \rho)\tan\alpha}$$

The residual transport q_{res} is decomposed in x and y direction using residual flow in vector form as in:

$$q_{res,x} = q_{res} \frac{\bar{u}_{r,x}}{\bar{u}_r}$$

$$q_{res,y} = q_{res} \frac{\bar{u}_{r,y}}{\bar{u}_r}$$

[34] Using the computed phases and amplitudes of the O_1, K_1, and M_2 constituents, and the residual flow visualized in Figure 11, these equations are applied in to compute the net transport of sediment due to tidal asymmetry and due to residual flow with tidal stirring (Figure 12). These results should be interpreted with care, because the amplitude of the M_2 current and the value of θ, and hence the sediment transport by tidal asymmetry, is overestimated by the model. At the same time, the residual flow is underestimated because we now only use the residual flow, and not the subtidal flows (mainly due to S_A, S_{SA}, KO_0, MS_0). Furthermore, sediment in Singapore's coastal waters is relatively fine-grained, and therefore its transport does not adapt instantaneously to the flow. The absolute transport rates are then not accurate due to the simple formula used for the sediment transport.

[35] Nevertheless, the results do provide information on the relative role of residual flows and tidal asymmetry, and on spatial changes thereof. Throughout the Singapore Strait, transport by tidal asymmetry is directed eastward while transport by residual flow is directed westward (Figures 12a and 12b). The magnitude of both computed transport components is of the same order of magnitude. Highest sediment transport occurs in areas with highest flow velocities, just south of the Southern Islands. The computed transport in the area of the Southern Islands is an order of magnitude lower than in the Singapore Strait. But as in the Singapore Strait, the computed contribution of residual flow and tidal asymmetry (Figures 12c and 12d) is comparable and in opposite direction. An exception is the area in the Northeast of the Southern Islands, where both residual flows and tidal asymmetry generate a net eastward transport. Close to the location of Sawa Buoy, transport due to residual flow is low while eastward transport due to tidal asymmetry is substantial. South of the Tuas extension (the most western large construction in Figures 12c and 12d), eastward transport due to tidal asymmetry is low whereas westward transport due to residual flow is strong.

[36] The fine sediment transport patterns computed with the full sediment transport model (approximating the residual transport) shows good agreement with the analytically computed transport by residual flow (compare Figure 12b and 12d with Figures 13b and 13d). The magnitude of the transport differs (as expected), but the direction of transport, and aerial distribution of transport magnitude is similar. The sand transport computed with the full transport model (Figures 13a and 13c) is more difficult to compare with transport by tidal asymmetry (Figures 12a and 13c) because the first is also strongly influenced by residual flow. Therefore the sand transport model reproduces the tidal asymmetry transport patterns best in areas where transport by residual flow is low: the pronounced eastward transport in the eastern part of the Singapore Strait (Figure 13a), and in

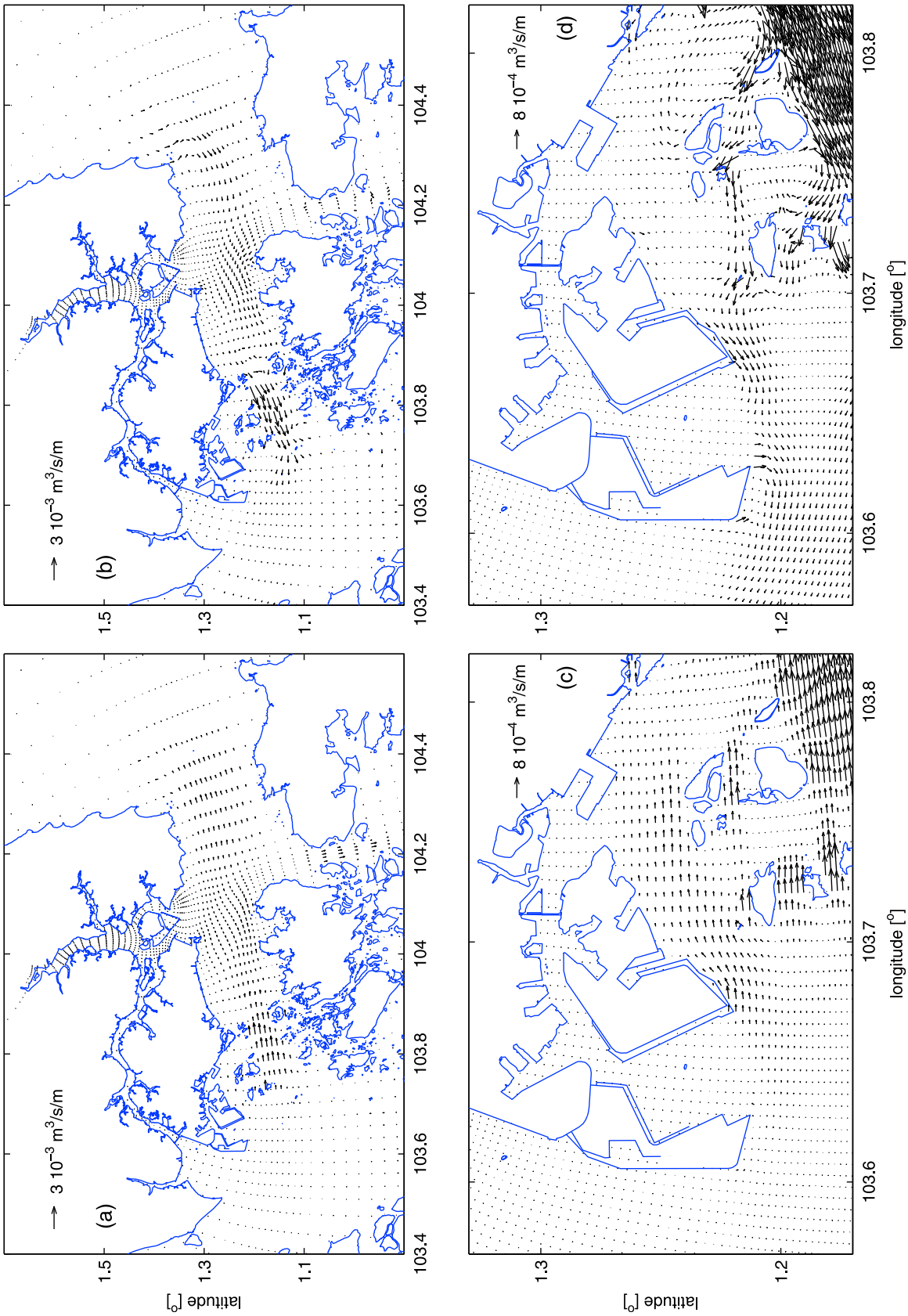

Figure 12. Residual transport (a, c) by tidal asymmetry and (b, d) by residual flow with tidal stirring around Singapore (Figures 12a and 12b) and in the in the Southern Islands area (Figures 12c and 12d). Vectors are shown every 3 grid cells (large domain) to 9 grid cells (refined domain) in Figures 12a and 12b, every grid cells in Figures 12c and 12d.

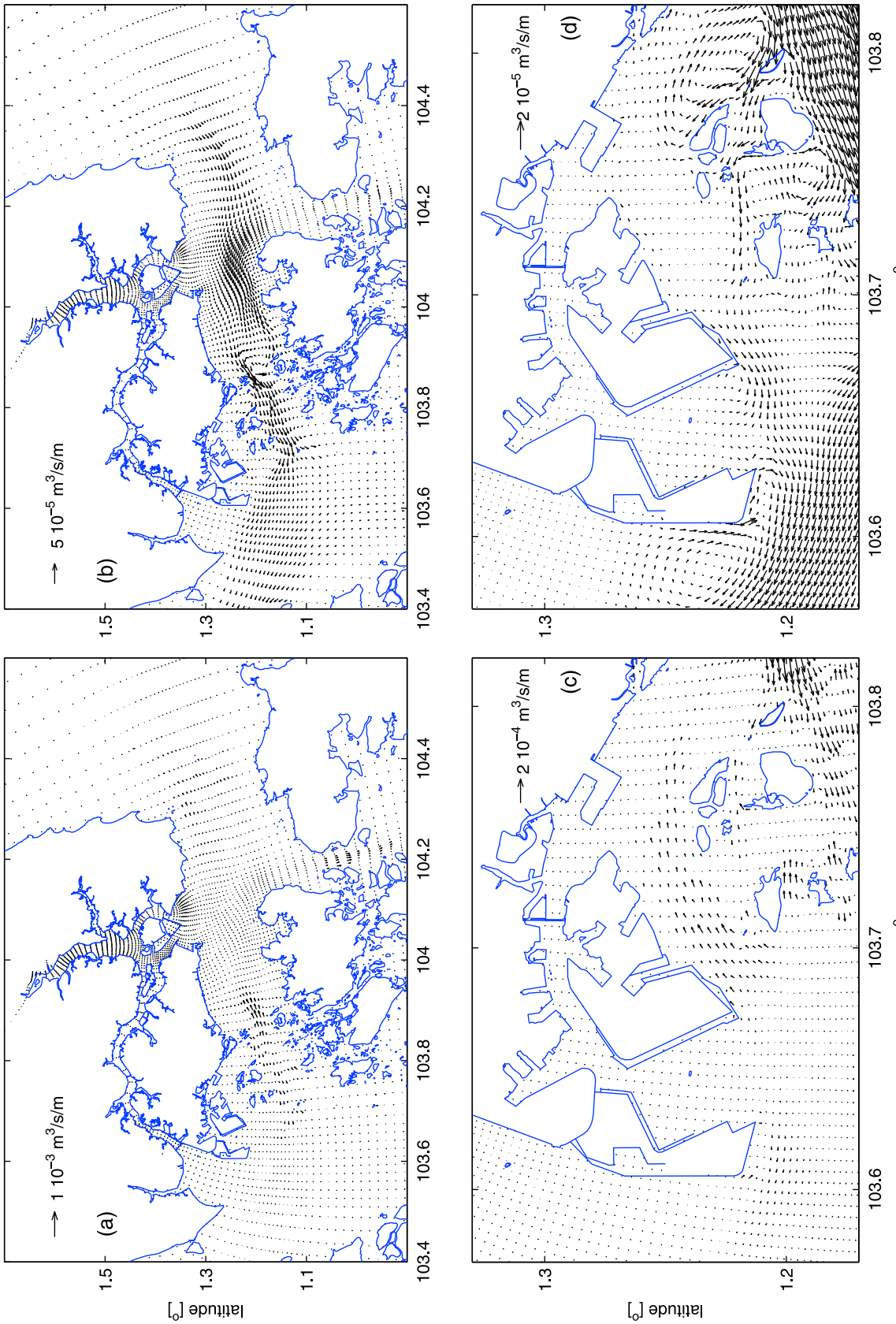

Figure 13. Transport of (a, c) sand and (b, d) fines around Singapore (Figures 13a and 13b) and in the in the Southern Islands area (Figures 13c and 13d). Vectors are shown every 3 grid cells (large domain) to 9 grid cells (refined domain) in Figures 13a and 13b, every grid cells in Figures 13c and 13d.

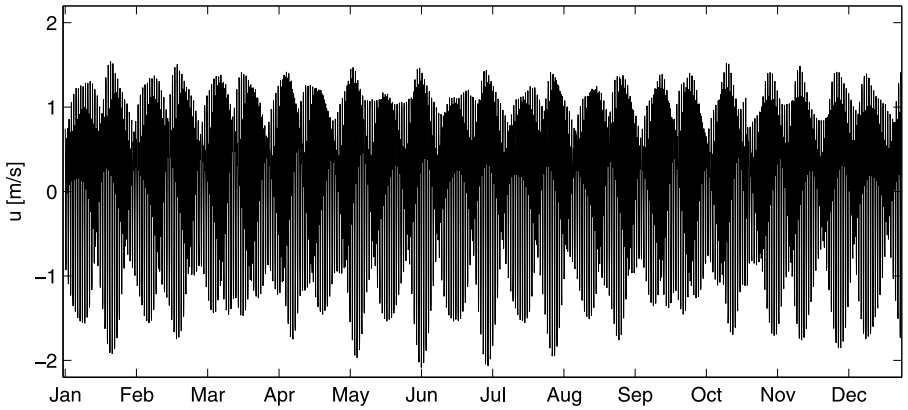

Figure 14. Harmonic reproduction of flow velocities at Charlotte Harbour, Boca Grande Pass, Florida, in 2004. Data from *WXTide32* [2007].

the Southern Islands region (Figure 13c). Transport by residual flow is stronger in the western part of the Singapore Strait: here the computed sand transport is in the westward direction (in contrast with the transport by tidal asymmetry alone).

5. Discussion

[37] The work presented here shows that tidal asymmetry in a mixed tidal regime is stronger than commonly observed in purely semidiurnal shelf seas of temperate regions, where asymmetry is dominated by M_2-M_4; only in some estuaries do equally pronounced asymmetries result from the M_2-M_4 interaction. However, the O_1-K_1-M_2 asymmetry is commonly found in (sub) tropical areas which are also typically influenced by pronounced subtidal flows, potentially promoting transports in opposite direction which may even exceed those due to tidal asymmetry. This may also lead to pronounced divergence of transport directions, depending on the grain size. Sediment in Singapore's coastal waters consists of mud, silt and sand. The finest sediment fraction is probably most sensitive to transport by residual flow, while sand transport may be more strongly influenced by tidal asymmetry. In areas with relatively low flow velocities, such as some sheltered areas in-between the islands in Figure 13, settling and scour lags may also substantially contribute to residual transport of fine sediment [*van Straaten and Kuenen*, 1957*; Postma*, 1961]. Nevertheless, transport due to residual flow is primarily in the westward direction while transport due to tidal asymmetry is primarily in the eastward direction. Therefore near Singapore, the finest sediment may be transported westward, while the coarser fraction is transported eastward.

[38] In areas where diurnal tides prevail, erosion-deposition patterns may be dictated by the diurnal spring-neap tidal cycle [*Kvale*, 2006]. Even more, interaction of the semidiurnal spring neap cycle and the diurnal spring neap cycle may play an important role for seasonal variations in turbidity and transport. Spring tides peak 2 times per year, and have minimal values every three month in-between. Additionally, pronounced tidal asymmetries may be generated of which the flow velocity and resulting transport is equal to or exceeds strong Monsoon-induced subtidal and residual currents. Near Singapore, periods during which tidal current velocities peak always coincide with periods of maximum Monsoon currents (either in westward (July) or eastward (December) direction). An inter-annual variation in spring tidal currents as pronounced as near Singapore can be expected in all diurnal or mixed, mainly diurnal tidal regimes. Even the phasing of this inter-annual variation is similar; spring tidal currents peak around January and July throughout the South China Sea but also in other diurnal tidal regimes (e.g., see the Gulf of Mexico in Figure 14). The wind patterns in the main areas where diurnal tides are prevalent (NW Australia, South China Sea, Gulf of Mexico) are dictated by the Monsoons. In these areas, yearly variations in turbidity are often associated with the Monsoons, resulting from the distinct seasonal variation in discharge, residual flows, and wave climate. However, since the interaction of the O_1-K_1 and M_2-S_2 spring-neap cycle gives rise to an equally distinct seasonal variation in peak tidal currents and asymmetries, the turbidity in these areas will at least partly result from tides alone as well. Especially throughout the South China Sea, maximum tidal asymmetry occurs simultaneously with peak Monsoon currents.

6. Conclusions

[39] The tidal and subtidal flows around Singapore are extremely complex, with substantial subtidal flows generated by residuals and low frequency currents with periodicities of 2 weeks to 1 year. The low-frequency currents are generated by both meteorological effects and by compound tides, and may exceed tidal currents during neap tide. The tidal water levels are mixed, semidiurnal while currents are mixed, diurnal to fully diurnal in areas influenced by large-scale tidal behavior. Currents may become fully semidiurnal in areas where the semidiurnal tide is mainly determined by local interaction with strongly varying bathymetry and geometry. The phase inclination of the three largest astronomical constituents (O_1-K_1-M_2) produces a strong and persistent tidal asymmetry, with maximum flow velocities opposite to the direction of residual flow. An analytical expression derived to estimate the relative importance of the residual flow and tidal asymmetry suggests that both are approximately evenly important. Fine sediment is most likely dominated by residual flow, and transported westward, while coarser sediment may be more strongly

influenced by tidal asymmetry and transported in opposite direction. In addition, the interaction of the diurnal spring-neap tidal cycle with the semidiurnal spring-neap cycle produces a distinct seasonal variation of peak tidal currents and asymmetries. This variation may substantially influence annual cycles of increased turbidity in diurnal and mixed tidal regimes.

[40] **Acknowledgments.** This work was carried out within Building with Nature project SI 4.3 "Supportive Modeling" and within the Singapore-Delft Water Alliance project "Large-scale sediment transport and turbidity in the Singapore coastal waters" funded by Deltares and EWI. We thank MPA for providing the local maritime data for analysis. The constructive comments of Nick Nidzieko and Ton Hoitink greatly improved this manuscript.

References

Arakawa, A., and V. R. Lamb (1977), Computational design of the basic dynamical process of the UCLA general circulation model, *Methods Comput. Phys.*, *17*, 173–265.

Aubrey, D. G. (1986), Hydrodynamic controls on sediment transport in well-mixed bays and estuaries, in *Physics of Shallow Estuaries and Bays*, edited by J. van de Kreeke, pp. 245–258, Springer, Berlin.

Bagnold, R. A. (1966), An approach to the sediment transport problem from general physics, *U.S. Geol. Surv. Prof. Pap.*, *422-I*, 37 pp.

Cronin, K., and D. S. van Maren (2011), Comparison of observed versus modeled current harmonic constituents in Singapore Strait, *Deltares Rep. 1201442-000*, 29 pp., Delft, Netherlands.

Dronkers, J. (1986), Tidal asymmetry and estuarine morphology, *Neth. J. Sea Res.*, *20*, 117–131, doi:10.1016/0077-7579(86)90036-0.

Egbert, G. D., and S. Y. Erofeeva (2002), Efficient inverse modeling of barotropic ocean tides, *J. Atmos. Oceanic Technol.*, *19*, 183–204, doi:10.1175/1520-0426(2002)019<0183:EIMOBO>2.0.CO;2.

Egbert, G. D., and R. D. Ray (2003), Deviation of long-period tides from equilibrium: Kinematics and geostrophy, *J. Phys. Oceanogr.*, *33*, 822–839, doi:10.1175/1520-0485(2003)33<822:DOLTFE>2.0.CO;2.

Friedrichs, C. T., and D. G. Aubrey (1988), Non-linear tidal distortion in shallow well-mixed estuaries: A synthesis, *Estuarine Coastal Shelf Sci.*, *27*, 521–545, doi:10.1016/0272-7714(88)90082-0.

Gerritsen, H., D. J. Twigt, A. Mynett, C. Calkoen, and V. Babovic (2009), MHBox—Analysis and prediction of sea level anomalies and associated currents in Singapore and Malacca Straits, paper presented at 8th International Conference on Hydroinformatics, Int. Cent. for Water Hazard Risk Manage., Concepción, Chile, Jan.

Godin, G. (1972), *The Analysis of Tides*, 264 pp., Liverpool Univ. Press, Liverpool, U. K.

Gordon, A. L. (2005), Oceanography of the Indonesian Seas and their throughflow, *Oceanography*, *18*, 14–27, doi:10.5670/oceanog.2005.01.

Hasan, G. M. J., D. S. van Maren, and H. F. Cheong (2012), Improving hydrodynamic modeling of an estuary in a mixed tidal regime by grid refining and aligning, *Ocean Dyn.*, *62*, 395–409, doi:10.1007/s10236-011-0506-4.

Hatayama, T., T. Awaji, and A. Akitomo (1996), Tidal currents in the Indonesian Seas and their effect on transport and mixing, *J. Geophys. Res.*, *101*, 12,353–12,373, doi:10.1029/96JC00036.

Hoitink, A. J. F. (2008), Comment on "The origin of neap–spring tidal cycles" by Erik P. Kvale [Marine Geology 235(2006) 5–18], *Mar. Geol.*, *248*, 122–125, doi:10.1016/j.margeo.2007.04.001.

Hoitink, A. J. F., and P. Hoekstra (2003), Hydrodynamic control of the supply of reworked terrigeneous sediment to coral reefs in the Bay of Banten (NW Java, Indonesia), *Estuarine Coastal Shelf Sci.*, *58*, 743–755, doi:10.1016/S0272-7714(03)00181-1.

Hoitink, A. J. F., P. Hoekstra, and D. S. Van Maren (2003), Flow asymmetry associated with astronomical tides: Implications for the residual transport of sediment, *J. Geophys. Res.*, *108*(C10), 3315, doi:10.1029/2002JC001539.

Jewell, S. A., D. J. Walker, and A. B. Fortunato (2012), Tidal asymmetry in a coastal lagoon subject to a mixed tidal regime, *Geomorphology*, *138*, 171–180, doi:10.1016/j.geomorph.2011.08.032.

Kow, T. A. (1973), *Seasonal distribution of the Plankton in the Singapore Straits, MBAI special publication dedicated to Dr. N. K. Panikkar*, pp. 60–73, Mar. Biol. Assoc. India, Tamil Nadu.

Kurniawan, A., S. K. Ooi, S. Hummel, and H. Gerritsen (2011), Sensitivity analysis of the tidal representation in Singapore regional waters in a data assimilation environment, *Ocean Dyn.*, *61*, 1121–1136, doi:10.1007/s10236-011-0415-6.

Kvale, E. P. (2006), The origin of neap-spring tidal cycles, *Mar. Geol.*, *235*, 5–18, doi:10.1016/j.margeo.2006.10.001.

Longuet-Higgins, M. S. (1953), Mass transport in water waves, *Philos. Trans. R. Soc. London, Ser. A*, *245*, 535–581, doi:10.1098/rsta.1953.0006.

Mazzega, P., and M. Berge (1994), Ocean Tides in the Asian semienclosed seas from TOPEX/POSEIDON, *J. Geophys. Res.*, *99*, 24,867–24,881, doi:10.1029/94JC01756.

Nidzieko, N. J. (2010), Tidal asymmetry in estuaries with mixed semidiurnal/diurnal tides, *J. Geophys. Res.*, *115*, C08006, doi:10.1029/2009JC005864.

O'Callaghan, J. M., C. B. Pattiaratchi, and D. P. Hamilton (2010), The role of intratidal oscillations in sediment resuspension in a diurnal, partially mixed estuary, *J. Geophys. Res.*, *115*, C07018, doi:10.1029/2009JC005760.

Ooi, S. K., P. Zemskyy, P. Sisomphon, H. Gerritsen, and D. J. Twigt (2009), The effect of grid resolution and weather forcing on hydrodynamic modelling of South East Asian waters, paper presented at 33rd International Association of Hydraulic Engineering and Research Biennial Congress, Vancouver, B. C., Canada, 9–14 Aug.

Ooi, S. K., H. Gerritsen, A. Kurniawan, and D. J. Twigt (2010), Parameter optimization and data assimilation to improve the tidal prediction of the Singapore regional model, paper presented at 17th Congress of the International Association of Hydraulic Engineering and Research-Asia and Pacific Division, Auckland, New Zealand, 21–24 Feb.

Pawlowicz, R., R. Beardsley, and S. Lentz (2002), Classical tidal harmonic analysis including error estimates in MATLAB using T TIDE, *Comput. Geosci.*, *28*, 929–937, doi:10.1016/S0098-3004(02)00013-4.

Postma, H. (1961), Transport and accumulation of suspended matter in the Dutch Wadden Sea, *Neth. J. Sea Res.*, *1*, 148–190, doi:10.1016/0077-7579(61)90004-7.

Potemra, J. T., S. L. Hautala, J. Sprintall, and W. Pandoe (2002), Interaction between the Indonesian Seas and the Indian Ocean in observations and numerical models, *J. Phys. Oceanogr.*, *32*, 1838–1854, doi:10.1175/1520-0485(2002)032<1838:IBTISA>2.0.CO;2.

Pugh, D. T. (1987), *Tides, Surges, and Mean Sea Level*, 472 pp., John Wiley, New York.

Ranasinghe, R., and C. Pattiaratchi (2000), Tidal inlet velocity asymmetry in diurnal regimes, *Cont. Shelf Res.*, *20*, 2347–2366, doi:10.1016/S0278-4343(99)00064-3.

Ray, R. D., G. D. Egbert, and S. Y. Erofeeva (2005), A brief overview of tides in the Indonesian Seas, *Oceanography*, *18*, 74–79, doi:10.5670/oceanog.2005.07.

Ridderinkhof, S. (1997), The effect of tidal asymmetries on the net transport of sediments in the Ems Dollard estuary, *J. Coastal Res.*, *25*, 41–48.

Robertson, R. (2011), Interaction between tides and other frequencies in the Indonesian Seas, *Ocean Dyn.*, *61*, 69–88, doi:10.1007/s10236-010-0343-x.

Robertson, R., and A. Field (2005), M2 baroclinic tides in the Indonesian Seas, *Oceanography*, *18*, 62–73, doi:10.5670/oceanog.2005.06.

Robinson, R. A., H. Tong, and T. A. Kow (1953), A study of drift in the Malacca and Singapore Straits from salinity determinations, *IPFC Proc.*, *4*, 105–110.

Schrama, E. J. O., and R. D. Ray (1994), A preliminary tidal analysis of TOPEX/ POSEIDON altimetry, *J. Geophys. Res.*, *99*, 24,799–24,808, doi:10.1029/94JC01432.

Seim, H. E., and J. E. Sneed (1988), Enhancement of semidiurnal tidal currents in the tidal inlets to Mississipi Sound, in *Hydrodynamics and Sediment Dynamics of Tidal Inlets. Lecture Notes on Coastal and Estuarine Studies*, edited by D. G. Aubrey and L. Weishar, pp. 157–168, Springer, Berlin.

Song, D., X. H. Wang, A. E. Kiss, and X. Bao (2011), The contribution to tidal asymmetry by different combinations of tidal constituents, *J. Geophys. Res.*, *116*, C12007, doi:10.1029/2011JC007270.

Stelling, G. S. (1984), *On the construction of computational methods for shallow water flow problems, PhD dissertation*, Delft Univ. of Technol., Hague, Netherlands.

Stelling, G. S., and J. J. Leendertse (1992), Approximation of convective processes by cyclic ADI methods, in *Estuarine and Coastal Modelling*, edited by M. L. Spaulding et al., pp. 771–782, Am. Soc. of Civ. Eng., New York.

Tarya, A., A. J. F. Hoitink, and M. Van Der Vegt (2010), Tidal and subtidal flow patterns on a tropical continental shelf semi-insulated by coral reefs, *J. Geophys. Res.*, *115*, C09029, doi:10.1029/2010JC006168.

van de Kreeke, J., and K. Robaczewska (1993), Tide-induced residual transport of coarse sediment; application to the Ems Estuary, *Neth. J. Sea Res.*, *31*, 209–220, doi:10.1016/0077-7579(93)90022-K.

van Maren, D. S., and P. Hoekstra (2004), Seasonal variation of hydrodynamics and sediment dynamics in a shallow subtropical estuary: The Ba

Lat River, Vietnam, *Estuarine Coastal Shelf Sci.*, *60*, 529–540, doi:10.1016/j.ecss.2004.02.011.

van Maren, D. S., P. Hoekstra, and A. J. F. Hoitink (2004), Tidal flow asymmetry in the diurnal regime: Bed load transport and morphologic changes around the Red River Delta, *Ocean Dyn.*, *3–4*, 424–434.

van Rijn, L. C. (1993), *Principles of Sediment Transport in Rivers, Estuaries and Coastal Seas*, 715 pp., Aqua, Amsterdam.

van Straaten, L. M. J. U., and P. H. Kuenen (1957), Accumulation of fine grained sediments in the Dutch Wadden Sea, *Geol. Mijnbouw*, *19*, 329–354.

Wang, Z. B., M. C. J. L. Jeuken, H. Gerritsen, H. J. de Vriend, and B. A. Kornman (2002), Morphology and asymmetry of the vertical tide in the Westerschelde estuary, *Cont. Shelf Res.*, *22*, 2599–2609, doi:10.1016/S0278-4343(02)00134-6.

Woodworth, P. L., D. L. Blackman, D. T. Pugh, and J. M. Vassie (2005), On the role of diurnal tides in contributing to asymmetries in tidal probability distribution functions in areas of predominantly semi-diurnal tide, *Estuarine Coastal Shelf Sci.*, *64*, 235–240, doi:10.1016/j.ecss.2005.02.014.

WXTide32 (2007), WXTide32 software, version 4.7, release October 2007. [Available at http://wxtide32.com.]

Wyrtki, K. (1961), Physical Oceanography of the South East Asian Waters. Naga Report, vol. *2*, 195 pp., Univ. of Calif. Press, La Jolla, Calif.

Xu, Z. (2000), *Ellipse Parameters Conversion and Vertical Velocity Profiles for Tidal Currents*, 20 pp., Bedford Inst. Oceanogr., Dartmouth, Nova Scotia.

Ye, A. L., and I. S. Robinson (1983), Tidal dynamics in the South China Sea, *Geophys. J. R. Astron. Soc.*, *72*, 691–707, doi:10.1111/j.1365-246X.1983.tb02827.x.

Zimmerman, J. T. F. (1978), Topographic generation of residual circulation by oscillatory (tidal) currents, *Geophys. Astrophys. Fluid Dyn.*, *11*, 35–47, doi:10.1080/03091927808242650.

Zu, T., J. Gan, and S. Y. Erofeeva (2008), Numerical study of the tide and tidal dynamics in the South China Sea, *Deep Sea Res., Part I*, *55*, 137–154, doi:10.1016/j.dsr.2007.10.007.

H. Gerritsen and D. S. van Maren, Deltares, PO Box 177, NL-2600 MH Delft, Netherlands. (bas.vanmaren@deltares.nl)